

# Bulk high-temperature superconductivity in pressurized tetragonal $\text{La}_2\text{PrNi}_2\text{O}_7$

<https://doi.org/10.1038/s41586-024-07996-8>

Received: 2 April 2024

Accepted: 28 August 2024

Published online: 2 October 2024

 Check for updates

Ningning Wang<sup>1,2,8</sup>✉, Gang Wang<sup>1,2,8</sup>, Xiaoling Shen<sup>3,4,8</sup>, Jun Hou<sup>1,2,8</sup>, Jun Luo<sup>1,2</sup>, Xiaoping Ma<sup>1</sup>, Huaixin Yang<sup>1,2</sup>, Lifen Shi<sup>1,2</sup>, Jie Dou<sup>1,2</sup>, Jie Feng<sup>1,2</sup>, Jie Yang<sup>1,2</sup>, Yunqing Shi<sup>1,2</sup>, Zhian Ren<sup>1,2</sup>, Hanming Ma<sup>1,3</sup>, Pengtao Yang<sup>1,2</sup>, Ziyi Liu<sup>1,2</sup>, Yue Liu<sup>1,2</sup>, Hua Zhang<sup>1,2</sup>, Xiaoli Dong<sup>1,2</sup>, Yuxin Wang<sup>1,2</sup>, Kun Jiang<sup>1,2</sup>, Jiangping Hu<sup>1,2,5</sup>, Shoko Nagasaki<sup>3</sup>, Kentaro Kitagawa<sup>3</sup>, Stuart Calder<sup>6</sup>, Jiaqiang Yan<sup>7</sup>, Jianping Sun<sup>1,2</sup>, Bosen Wang<sup>1,2</sup>, Rui Zhou<sup>1,2</sup>✉, Yoshiya Uwatoko<sup>3</sup>✉ & Jinguang Cheng<sup>1,2</sup>✉

The Ruddlesden–Popper (R–P) bilayer nickelate,  $\text{La}_3\text{Ni}_2\text{O}_7$ , was recently found to show signatures of high-temperature superconductivity (HTSC) at pressures above 14 GPa (ref. 1). Subsequent investigations achieved zero resistance in single-crystalline and polycrystalline samples under hydrostatic pressure conditions<sup>2–4</sup>. Yet, obvious diamagnetic signals, the other hallmark of superconductors, are still lacking owing to the filamentary nature with low superconducting volume fraction<sup>2,4,5</sup>. The presence of a new 1313 polymorph and competing R–P phases obscured proper identification of the phase for HTSC<sup>6–9</sup>. Thus, achieving bulk HTSC and identifying the phase at play are the most prominent tasks. Here we address these issues in the praseodymium (Pr)-doped  $\text{La}_2\text{PrNi}_2\text{O}_7$  polycrystalline samples. We find that substitutions of Pr for La effectively inhibit the intergrowth of different R–P phases, resulting in a nearly pure bilayer structure. For  $\text{La}_2\text{PrNi}_2\text{O}_7$ , pressure-induced orthorhombic to tetragonal structural transition takes place at  $P_c \approx 11$  GPa, above which HTSC emerges gradually on further compression. The superconducting transition temperatures at 18–20 GPa reach  $T_c^{\text{onset}} = 82.5$  K and  $T_c^{\text{zero}} = 60$  K, which are the highest values, to our knowledge, among known nickelate superconductors. Importantly, bulk HTSC was testified by detecting clear diamagnetic signals below about 75 K with appreciable superconducting shielding volume fractions at a pressure of above 15 GPa. Our results not only resolve the existing controversies but also provide directions for exploring bulk HTSC in the bilayer nickelates.

The recent report on the signature of high-temperature superconductivity (HTSC) in the pressurized  $\text{La}_3\text{Ni}_2\text{O}_7$  crystals has increased the interest of researchers in the Ruddlesden–Popper (R–P) nickelates<sup>1–30</sup>,  $\text{La}_{n+1}\text{Ni}_n\text{O}_{3n+1}$  ( $n = 1, 2, 3, \dots, \infty$ ), which consists of alternatively stacked  $n\text{LaNiO}_3$  and  $\text{LaO}$  layers along the  $c$ -axis. As the Ni valence increases with  $n$ , stabilization of these R–P nickelates depends on the oxygen pressure ( $p_{\text{O}_2}$ ) (ref. 31). Previous studies have demonstrated difficulties in obtaining single-phase  $\text{La}_3\text{Ni}_2\text{O}_7$  crystals with a nominal  $\text{Ni}^{2+}$  state<sup>1,2,8,26,31,32</sup>. It is only within a narrow range of  $p_{\text{O}_2} \approx 10$ –18 bar that the  $\text{La}_3\text{Ni}_2\text{O}_7$  crystals with the majority  $n = 2$  (327) phase can be obtained<sup>1,6,8,33</sup>, coexisting with some minority  $n = 1$  (214) and  $n = 3$  (4310) phases. For these  $\text{La}_3\text{Ni}_2\text{O}_7$  crystals, a recent study shows considerable oxygen vacancies at inner apical O1 positions<sup>24</sup>. Apart from the bilayer 2222 phase, recent structural analyses showed a new 1313 polymorph featured by an alternative stacking of single- and triple-layer phases<sup>6–9</sup>; these 1313 crystals were found to show signatures of HTSC similar to the 2222 crystals<sup>6</sup>. These crystal imperfections and the presence of multiple structural variants obscured proper identification of the phase

responsible for HTSC. Under these circumstances, we recently resorted to the  $\text{La}_3\text{Ni}_2\text{O}_{7-\delta}$  polycrystalline samples, which can be prepared in a relatively large quantity with better-controlled quality and reproducibility by wet-chemistry sol-gel method<sup>4,32</sup>. This enabled us to perform comprehensive examinations of its crystal structure, oxygen content and transport properties under high pressure. For this sample, we can reproducibly achieve zero resistance with  $T_c^{\text{zero}}$  up to 40 K but did not observe discernible diamagnetic signals in a.c. magnetic susceptibility  $\chi'(T)$  up to 15 GPa (ref. 4). Our results reaffirmed the filamentary nature of the observed HTSC in  $\text{La}_3\text{Ni}_2\text{O}_{7-\delta}$ , whereas its origin remains unknown. As shown below, these mysteries should root in the considerable structural disorders in  $\text{La}_3\text{Ni}_2\text{O}_{7-\delta}$ .

## Stacking faults in $\text{La}_3\text{Ni}_2\text{O}_{7-\delta}$

In our recent work, we noted that the  $(h, k, 0)$  reflections of neutron powder diffraction (NPD) pattern of  $\text{La}_3\text{Ni}_2\text{O}_{7-\delta}$  are resolution limited, whereas those associated with the  $c$ -axis show clear

<sup>1</sup>Beijing National Laboratory for Condensed Matter Physics and Institute of Physics, Chinese Academy of Sciences, Beijing, China. <sup>2</sup>School of Physical Sciences, University of Chinese Academy of Sciences, Beijing, China. <sup>3</sup>Institute for Solid State Physics, University of Tokyo, Kashiwa, Chiba, Japan. <sup>4</sup>Key Laboratory of Artificial Structures and Quantum Control, School of Physics and Astronomy, Shanghai Jiao Tong University, Shanghai, China. <sup>5</sup>New Cornerstone Science Laboratory, Beijing, China. <sup>6</sup>Neutron Scattering Division, Oak Ridge National Laboratory, Oak Ridge, TN, USA. <sup>7</sup>Materials Science and Technology Division, Oak Ridge National Laboratory, Oak Ridge, TN, USA. <sup>8</sup>These authors contributed equally: Ningning Wang, Gang Wang, Xiaoling Shen, Jun Hou. <sup>✉</sup>e-mail: nnwang@iphy.ac.cn; rzhou@iphy.ac.cn; uwatoko@issp.u-tokyo.ac.jp; jgcheng@iphy.ac.cn

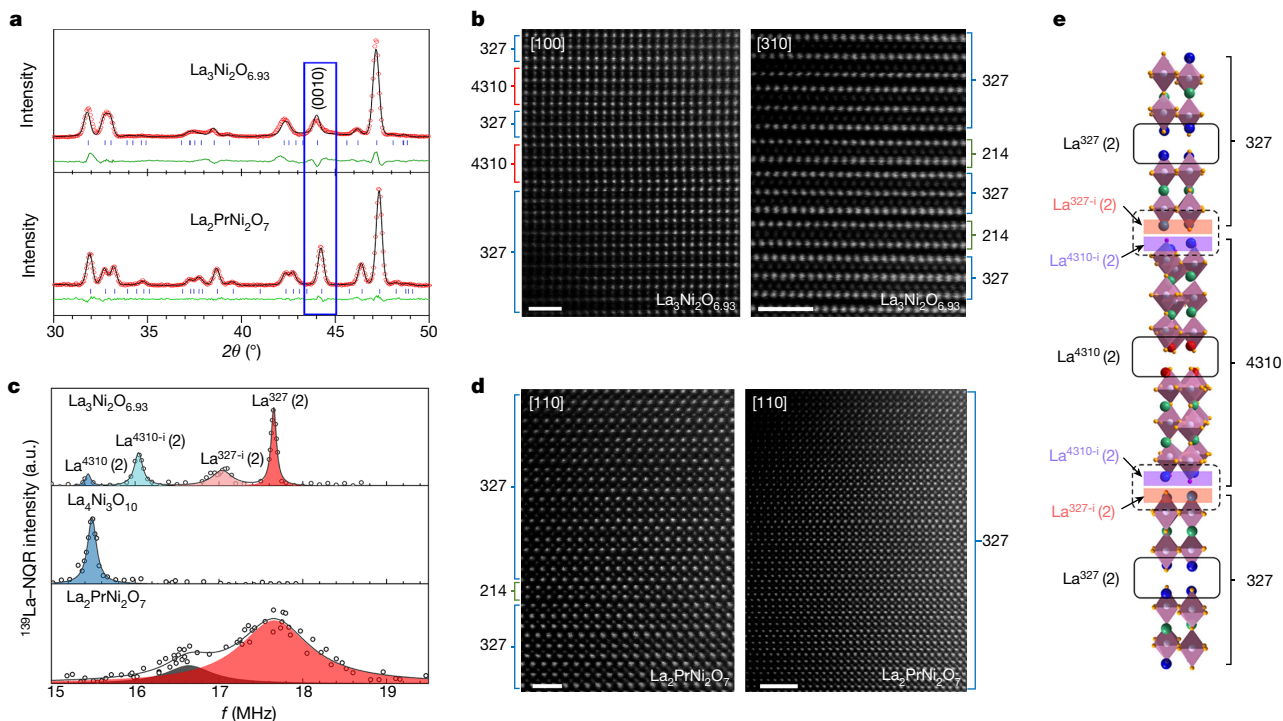


**Fig. 1 | Characterizations of the micro-structures of  $\text{La}_{3-x}\text{Pr}_x\text{Ni}_2\text{O}_{7-\delta}$  ( $x=0, 1$ ) samples.** **a**, Rietveld refinements of the NPD patterns in the  $2\theta$  range between  $30^\circ$  and  $50^\circ$ , highlighting the distinct features of the (0 0 10) reflection. The NPD data for  $x = 0$  sample were taken from ref. 4. **b,d**, HAADF-STEM images illustrating the stacking of layers along the  $c$ -axis for  $\text{La}_3\text{Ni}_2\text{O}_{7-\delta}$  (**b**) and  $\text{La}_2\text{PrNi}_2\text{O}_7$  (**d**) samples. **c**,  $^{139}\text{La}(2)$  NQR spectra around the frequency  $3\nu_Q$  in  $\text{La}_3\text{Ni}_2\text{O}_{7-\delta}$ ,  $\text{La}_4\text{Ni}_3\text{O}_{10}$  and  $\text{La}_2\text{PrNi}_2\text{O}_7$  samples at 188 K. The solid lines represent fits obtained using Lorentz functions. Pr doping inevitably induces structural disorders,

resulting in a significant broadening of the NQR spectrum by an order of magnitude. No peaks corresponding to the 4310 phase are observed for  $\text{La}_2\text{PrNi}_2\text{O}_7$ . A minor peak at 16.5 MHz might be attributed to the possible residual interfaces or the La sites adjacent to Pr. **e**, Schematic of the structure illustrating different  $\text{La}^{4310}(2)$ ,  $\text{La}^{4310i}(2)$ ,  $\text{La}^{327i}(2)$  and  $\text{La}^{327}(2)$  sites with triple-layer  $\text{NiO}_2$  intercalated in normal double-layer  $\text{NiO}_2$  plane. Scale bars, 1 nm (**b**, left and right; **d**, left); 2 nm (**d**, right).

asymmetric Warren-like shapes (Fig. 1a), which are typically attributed to short-range orders or stacking faults along the  $c$ -axis<sup>4</sup>. To verify this, we performed high-angle annular dark-field (HAADF) scanning transmission electron microscopy (STEM) on the  $\text{La}_3\text{Ni}_2\text{O}_{7-\delta}$  samples. Although the bilayer structure dominates in most images, we observe ubiquitous intergrowth of 327 with 4310 and 214 phases (Fig. 1b). This is not surprising considering the similar structural arrangement of these R-P phases. How these intergrowths affect the transport properties of  $\text{La}_3\text{Ni}_2\text{O}_{7-\delta}$ ; especially, pressure-induced HTSC is an intriguing issue that has been overlooked so far. To address this issue, we need to quantify the amount of stacking faults associated with the intergrowths. This is challenging for local probes such as STEM. We thus resorted to nuclear quadrupole resonance (NQR) as a sensitive global probe to investigate the local structure disorders of bulk samples.

Owing to the nuclear spin of  $^{139}\text{La}$  being  $7/2$ , we observed three sets of resonance peaks in the NQR spectrum (Extended Data Fig. 1). By comparing the quadrupole frequency  $\nu_Q \approx 5\text{--}6$  MHz with previous studies<sup>25,34</sup> (Extended Data Table 1), we determine that these three sets of resonance peaks correspond to the La(2) site. Notably, each set exhibits four peaks in the La(2) NQR spectrum (Fig. 1c, top), indicating the presence of four distinct La(2) sites. By comparing with the NQR spectrum of  $\text{La}_4\text{Ni}_3\text{O}_{10}$  (Fig. 1c, middle), the lowest frequency peak in the La(2) NQR spectrum of  $\text{La}_3\text{Ni}_2\text{O}_{7-\delta}$  should correspond to that of  $\text{La}_4\text{Ni}_3\text{O}_{10}$ . In combination with the STEM results, we propose that the intergrowth between 327 and 4310 phases will result in two new sites:  $\text{La}^{327i}(2)$  and  $\text{La}^{4310i}(2)$  (Fig. 1e). The  $\nu_Q$  values for these two new sites are expected to fall between those of  $\text{La}^{327}(2)$  and  $\text{La}^{4310}(2)$ , and their peaks should have equal areas owing to the same number of nuclei. Furthermore, owing to their positioning between two- and three-layer  $\text{NiO}_2$  interfaces, the anisotropy parameter  $\eta$  of the electrical field gradient should become larger compared with

$\text{La}^{327}(2)$  and  $\text{La}^{4310}(2)$ . The  $\eta$  values for the middle two peaks are much larger compared with those on either side (Extended Data Table 1). Moreover, the spectral weight ratio between  $\text{La}^{327i}(2)$  and  $\text{La}^{4310i}(2)$  is close to 1:1. These analyses indicate that the resonance peaks from low to high frequency in Fig. 1c (top) correspond to  $\text{La}^{4310}(2)$ ,  $\text{La}^{4310i}(2)$ ,  $\text{La}^{327i}(2)$  and  $\text{La}^{327}(2)$  sites. We did not observe the 214 phase in our NQR spectra at 188 K because it is antiferromagnetically ordered<sup>35,36</sup>, resulting in broad NQR lines and feeble signals<sup>37</sup>. Our study demonstrated that the  $\text{La}^{4310}(2)$  and  $\text{La}^{4310i}(2)$  account for around 30% of the NQR spectral weight (Extended Data Table 1), the small spectral weight of  $\text{La}^{4310}(2)$  suggests that trilayer-NiO<sub>2</sub> does not exhibit continuous stacking along the  $c$ -axis to form a real 4310 phase. This is elaborated by the STEM images in Fig. 1b. This short-range-ordered arrangement of 327/4310 and 327/214 interfaces along the  $c$ -axis makes it hard to detect by conventional XRD. Whether a similar situation occurs in the  $\text{La}_3\text{Ni}_2\text{O}_7$  crystals deserves further scrutiny. This observation raises an important question of whether these stacking faults or interfaces are responsible for the filamentary HTSC or detrimental to achieving bulk HTSC. To this end, it is essential to study 327-phase-pure samples. We show below that the substitutions of Pr for La in  $\text{La}_2\text{PrNi}_2\text{O}_{7-\delta}$  can effectively improve the phase purity.

### La<sub>2</sub>PrNi<sub>2</sub>O<sub>7-δ</sub> with improved phase purity

A series of  $\text{La}_{3-x}\text{Pr}_x\text{Ni}_2\text{O}_{7-\delta}$  ( $0 \leq x \leq 1$ ) polycrystalline samples were prepared using the sol-gel method (Methods). Here we focus on  $\text{La}_2\text{PrNi}_2\text{O}_{7-\delta}$  with the highest doping level that can maintain the orthorhombic *Amam* structure (Extended Data Fig. 2). In contrast to  $\text{La}_3\text{Ni}_2\text{O}_{7-\delta}$ , the asymmetric Warren-like feature of (0 0 10) peak is hardly discernible

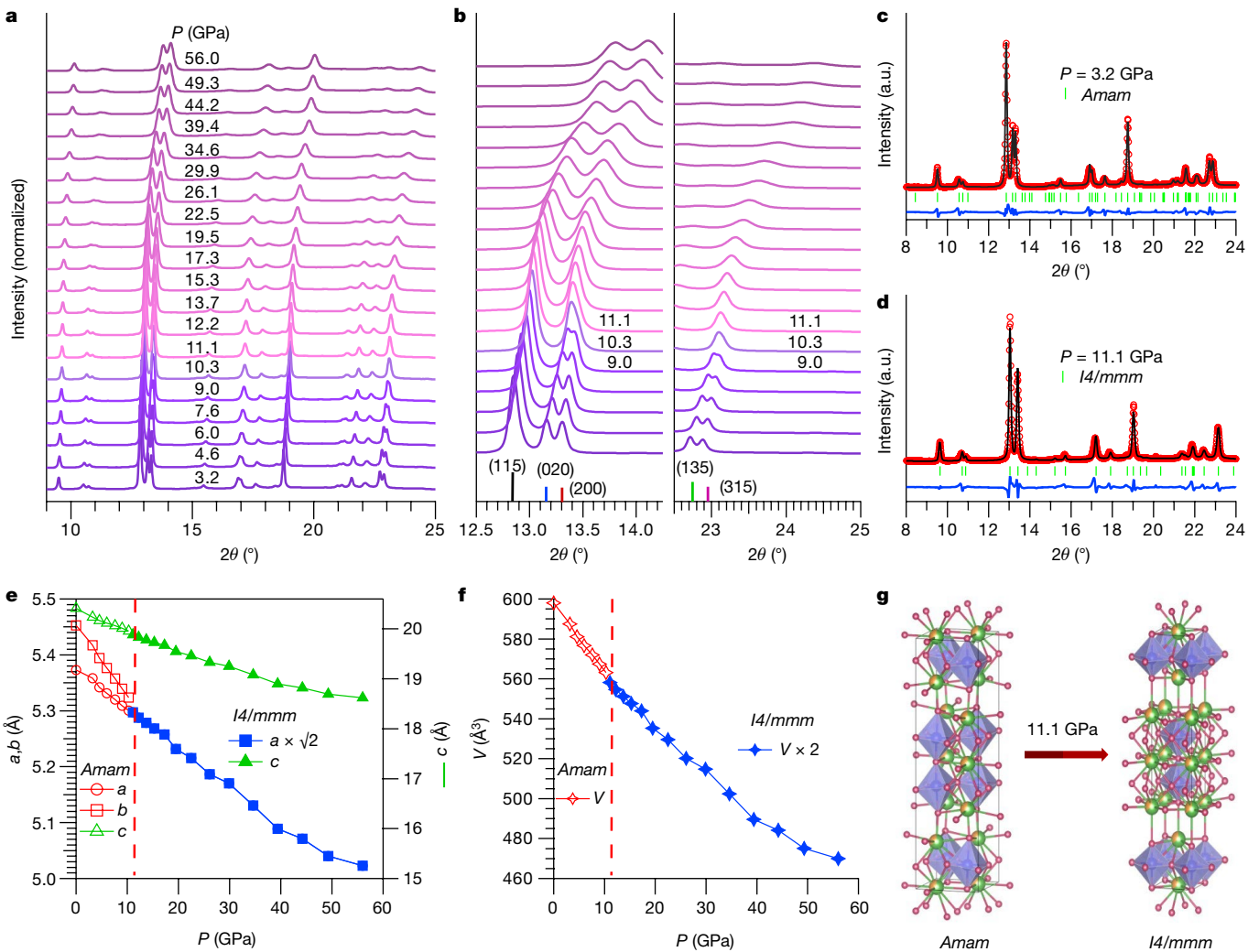


**Fig. 2 | Pressure-induced structural transition in  $\text{La}_2\text{PrNi}_2\text{O}_7$ .** **a**, SXRD patterns of  $\text{La}_2\text{PrNi}_2\text{O}_7$  powder samples under various pressures between 3.2 GPa and 56 GPa. **b**, The enlarged view of SXRD around the representative  $2\theta$  ranges highlights the gradual merging of the diffraction peaks on compression.

**c,d**, Refinement results of the SXRD patterns at 3.2 GPa using the space group *Amam* (**c**) and at 11.1 GPa using the space group *I4/mmm* (**d**). **e,f**, Lattice parameters (**e**) and cell volume (**f**) as a function of the pressure. **g**, Crystal structure transformation of  $\text{La}_2\text{PrNi}_2\text{O}_7$  under high pressure. a.u., arbitrary units.

for  $\text{La}_2\text{PrNi}_2\text{O}_{7-\delta}$  (Fig. 1a), signalling an obvious improvement of the quality of the sample. The refined unit-cell parameters of  $\text{La}_2\text{PrNi}_2\text{O}_{7-\delta}$  are smaller than those of  $\text{La}_3\text{Ni}_2\text{O}_{7-\delta}$  as expected, and the chemical pressure exerted by smaller  $\text{Pr}^{3+}$  on the overall lattice corresponds to an external pressure of around 2.5 GPa according to the experimental  $P$ - $V$  relationship. Unlike physical pressure, the substitutions of  $\text{Pr}^{3+}$  produce stronger orthorhombic distortions manifested by smaller Ni–O–Ni bond angles, which reduce the overlap integral between  $\text{Ni}-e_g$  and  $\text{O}-2p$  orbitals and result in higher resistivity as observed experimentally (Extended Data Fig. 3). The energy-dispersive X-ray spectroscopy (EDX) measurements confirm uniform distribution of elemental compositions, whereas thermogravimetric analysis (TGA) shows negligible oxygen deficiency  $\delta \approx 0.02(1)$ , consistent with the NPD refinement results (Extended Data Fig. 4 and Extended Data Table 2). Thus, we denoted the sample as  $\text{La}_2\text{PrNi}_2\text{O}_7$  hereafter.

The STEM images of  $\text{La}_2\text{PrNi}_2\text{O}_7$  show that the 327/4310 intergrowth can hardly be observed, and the 327/214 intergrowth is reduced, consistent with the NPD results (Fig. 1d). The absence of the 4310 phase was further verified by the NQR measurements. As shown in Fig. 1c (bottom), the resonance peaks for  $\text{La}^{4310}(2)$  and  $\text{La}^{4310i}(2)$  are absent, whereas a broad peak is observed at the  $\text{La}^{327}(2)$  position. The combined STEM and NQR results together with the NPD refinements unambiguously

verified the improved phase purity with negligible oxygen vacancies in the  $\text{La}_2\text{PrNi}_2\text{O}_7$  samples. Apart from the enhanced orthorhombic structural distortions, we speculate that the valence instability of the Pr ions at elevated temperatures might be a key factor for the elimination of the 4310 phase. More studies are needed to demonstrate the roles of Pr substitutions in  $\text{La}_3\text{Ni}_2\text{O}_{7-\delta}$ . The availability of nearly 327-phase-pure  $\text{La}_2\text{PrNi}_2\text{O}_7$  samples provides an excellent opportunity to clarify the roles of the 327/4310 interfaces for pressure-induced HTSC.

## Pressure-induced structural transition

For  $\text{La}_3\text{Ni}_2\text{O}_{7-\delta}$ , the emergence of HTSC is concomitant with the orthorhombic *Amam* to *Fmmm* structure transition under high pressure<sup>1</sup>. A recent high-pressure study shows that the sample adopts a tetragonal *I4/mmm* structure in the superconducting phase at low temperatures<sup>16</sup>. It is interesting to examine whether structural transition appears in  $\text{La}_2\text{PrNi}_2\text{O}_7$  under high pressure. Figure 2a shows the synchrotron XRD (SXRD) patterns collected at room temperature under various pressures from 3.2 GPa to 56 GPa. The SXRD patterns below 10.3 GPa consistently match the orthorhombic *Amam* structure, as shown in Fig. 2c for the representative refinement at 3.2 GPa. However, on compression to 11.1 GPa, several adjacent peaks are merged, such as

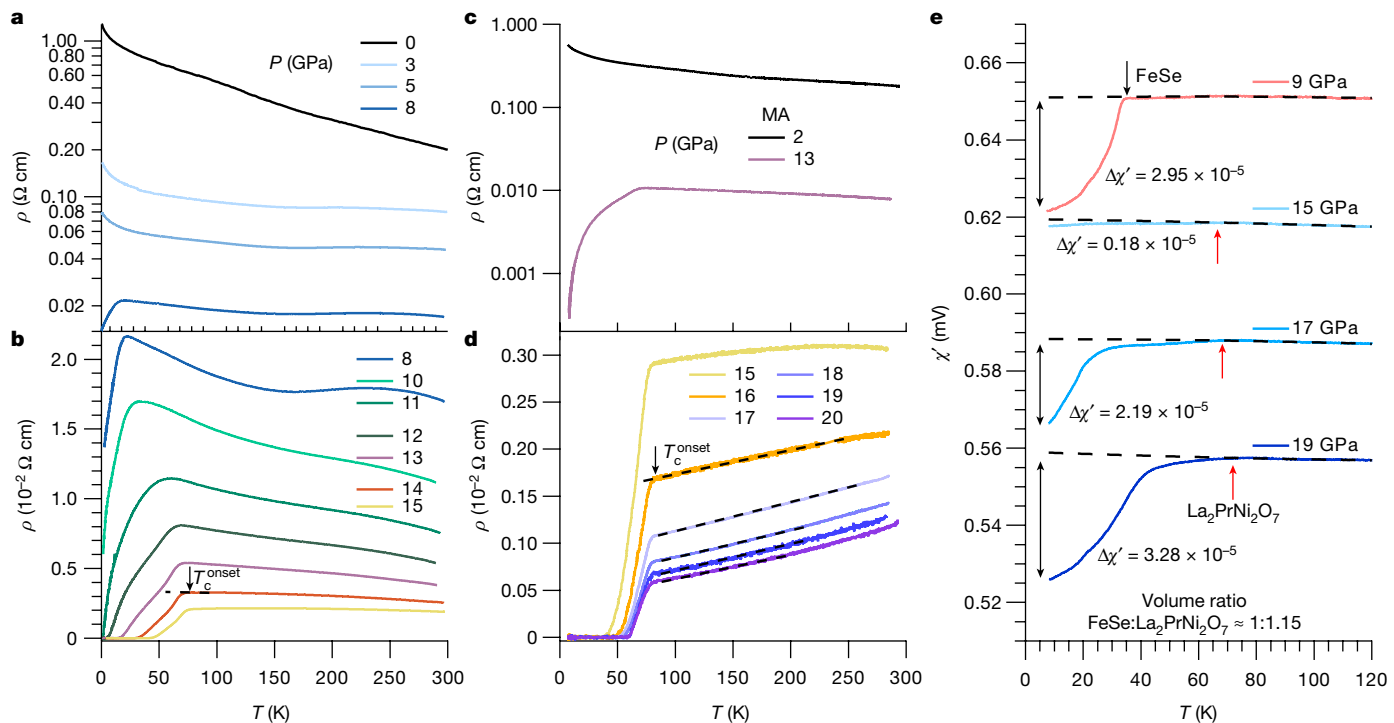


**Fig. 3 | Pressure-induced HTSC in the  $\text{La}_2\text{PrNi}_2\text{O}_7$ .** **a,b,**  $\rho(T)$  of sample 1 under various hydrostatic pressures up to 15 GPa measured in the cubic anvil cell (CAC) at the Institute of Physics, Chinese Academy of Sciences. Here,  $T_c^{\text{onset}}$  is determined as the interception between two straight lines below and above the superconducting transition. **c,d,**  $\rho(T)$  of sample 2 under various hydrostatic pressures up to 20 GPa measured in the multianvil (MA) at the Institute for

Solid State Physics, University of Tokyo. **e,**  $\chi'(T)$  of sample 3 under various pressures of up to 19 GPa measured with MA. The data at a pressure above 15 GPa show clear diamagnetic signals below approximately 70–75 K, unambiguously confirming the achievement of bulk HTSC. The dashed line represents the background extrapolated from the high-temperature region.

the (0 2 0) and (2 0 0) peaks at approximately  $13.4^\circ$  and the (1 3 5) and (3 1 5) peaks at approximately  $23.1^\circ$  (Fig. 2b). This observation suggests pressure-induced structural transition towards a higher symmetry. Subsequent analyses showed that the high-pressure phase can be better described using the  $\text{Sr}_3\text{Ti}_2\text{O}_7$ -type structural model with a tetragonal  $I4/mmm$  space group (Fig. 2d), especially at a pressure above 15 GPa (Extended Data Fig. 5).

As shown in Fig. 2e,f, the lattice parameters of  $\text{La}_2\text{PrNi}_2\text{O}_7$  decrease smoothly with increasing pressure but exhibit anisotropic compressions. In the lower pressure range,  $b$  decreases faster than  $a$  and they merge at 11.1 GPa, at which the structural transition takes place. This orthorhombic *Amam* to tetragonal  $I4/mmm$  structural transition (Fig. 2g) is distinct from that observed in  $\text{La}_3\text{Ni}_2\text{O}_7$  crystals in which the high-pressure phase adopts the orthorhombic *Fmmm* symmetry at room temperature.

## Emergence of HTSC

To explore HTSC in the high-pressure tetragonal phase of  $\text{La}_2\text{PrNi}_2\text{O}_7$ , we measured resistivity  $\rho(T)$  of sample 1 with cubic anvil cell (CAC) apparatus under various hydrostatic pressures up to 15 GPa. In Fig. 3a,  $\rho(T)$  at 0 GPa exhibits a typical semiconducting behaviour throughout the entire temperature range because of enhanced local structural distortions as discussed above. On compression, the magnitude of  $\rho(T)$  decreases monotonically in the entire temperature range but retains a semiconducting-like behaviour up to 5 GPa. When pressure is increased to 8 GPa, approaching the pressure of structural transition, a clear drop in  $\rho(T)$  is observed below 21.4 K (Fig. 3b). This behaviour becomes more pronounced as pressure increases, signalling the appearance of superconductivity. At 12 GPa,  $\rho(T)$  reaches zero resistance at 4.4 K with  $T_c^{\text{onset}} = 66.4$  K.  $T_c^{\text{zero}}$  increases rapidly to 40 K at 15 GPa at which  $T_c^{\text{onset}}$  reaches 78.2 K. The emergence of HTSC in

$\text{La}_2\text{PrNi}_2\text{O}_7$  is coincident with the structural transition as observed in  $\text{La}_3\text{Ni}_2\text{O}_7$  (ref. 1).

To confirm the reproducibility of the above results and to track  $T_c$  to higher pressures, we measured  $\rho(T)$  on sample 2 up to 20 GPa by using a two-stage 6/8 multianvil (MA) apparatus. As seen in Fig. 3c,d,  $\rho(T)$  values at  $P \leq 15$  GPa are consistent with those of sample 1, and  $\rho(T)$  at  $P \geq 16$  GPa transform into metallic behaviour with the normal state characterized by a  $T$ -linear strange-metal behaviour over a wide temperature range. Similar behaviours were observed in  $\text{La}_3\text{Ni}_2\text{O}_7$  (refs. 1,3,4), implying an intimate relationship between the strange-metal behaviour and HTSC in this system. Meanwhile,  $T_c^{\text{onset}}$  increases to 82.5 K at 16 GPa and then decreases slightly to 80.4 K at 20 GPa, whereas  $T_c^{\text{zero}}$  increases rapidly from 36.3 K at 15 GPa to about 60 K at 19–20 GPa. The negative effects of magnetic field and electrical current on  $\rho(T)$  below  $T_c^{\text{onset}}$  (Extended Data Fig. 6) further elaborate on the occurrence of HTSC. Notably,  $\text{La}_2\text{PrNi}_2\text{O}_7$  exhibits record-high  $T_c^{\text{zero}} \approx 60$  K among known nickelate superconductors, which is about 20 K higher than that of  $\text{La}_3\text{Ni}_2\text{O}_{7-\delta}$  at a similar pressure. These results demonstrate that the absence of 327/4310 interfaces is beneficial for achieving superior superconducting properties, which is further substantiated by the observation of apparent diamagnetic signals below.

## Evidence of bulk HTSC

Figure 3e shows  $\chi'(T)$  of  $\text{La}_2\text{PrNi}_2\text{O}_7$  sample 3 together with a piece of FeSe single crystal as a reference. The superconducting diamagnetic response of FeSe at 9 GPa is clearly visible, consistent with our previous studies<sup>38,39</sup>. As FeSe undergoes a structural transition at about 10 GPa into a non-superconducting hexagonal phase<sup>40,41</sup>, the observed diamagnetic signals in  $\chi'(T)$  above 15 GPa should be attributed to  $\text{La}_2\text{PrNi}_2\text{O}_7$ . By comparing with the background line superposed on each  $\chi'(T)$  curve, we can see the diamagnetic signal of  $\text{La}_2\text{PrNi}_2\text{O}_7$ , which starts to appear below

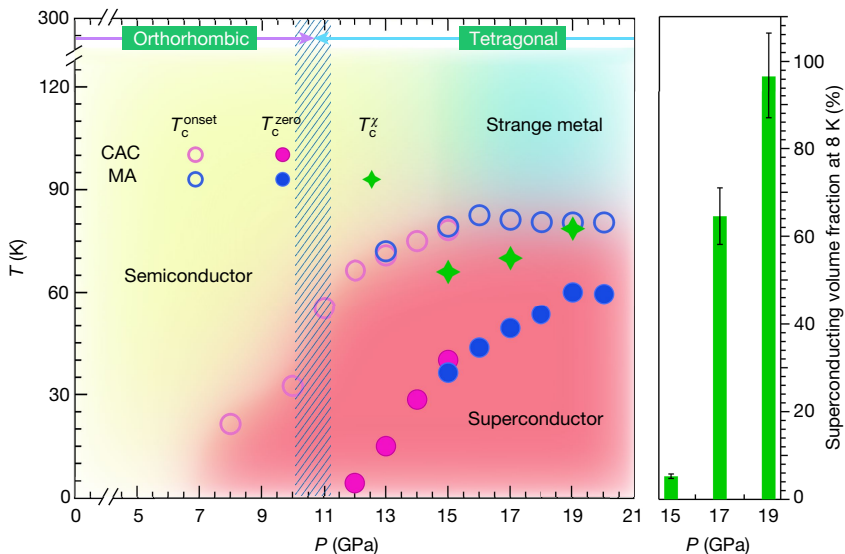


**Fig. 4 |  $T$ - $P$  phase diagram of  $\text{La}_2\text{PrNi}_2\text{O}_7$ .** The open and closed circles represent the onset and zero-resistance superconducting transition temperatures,  $T_c^{\text{onset}}$  and  $T_c^{\text{zero}}$ , determined from the  $\rho(T)$  measurements in the cubic anvil cell (CAC) and multianvil (MA). The star represents the  $T_c^\chi$  determined from  $\chi'(T)$

measurements in the multianvil. The bar chart on the right represents the estimated superconducting shielding volume fraction,  $f_{\text{sc}}$ , at 8 K under different pressures. The error bar is estimated to be about 10%.

around 65 K at 15 GPa and gets stronger with increasing pressure. Owing to the polycrystalline nature of the  $\text{La}_2\text{PrNi}_2\text{O}_7$  samples, its diamagnetic response of  $\chi'(T)$  at  $T_c$  is not as sharp as FeSe but develops gradually below  $T_c$  accompanying the progressive enhancement of long-range coherence for Cooper pairing on cooling down. The superconducting shielding volume fraction,  $f_{\text{sc}}$ , of  $\text{La}_2\text{PrNi}_2\text{O}_7$  can be estimated by comparing its diamagnetic response to that of FeSe at 9 GPa, which is confirmed to be  $f_{\text{sc}} \approx 100\%$  (Extended Data Fig. 7b). Considering the volume ratio of about 1:1.15 between FeSe and  $\text{La}_2\text{PrNi}_2\text{O}_7$ , the  $f_{\text{sc}}$  of  $\text{La}_2\text{PrNi}_2\text{O}_7$  at 8 K is estimated to increase rapidly from approximately 5.3(5)% at 15 GPa to approximately 97(10)% at 19 GPa. Measurements of  $\chi'(T)$  on sample 4 reproduced the above results, yielding an  $f_{\text{sc}}$  of about 57(6)% at 20 GPa (Extended Data Fig. 7c). Despite sample-dependent behaviours, the observations of  $f_{\text{sc}}$  of about 97(10)% and 57(6)% for two independent measurements unambiguously testified to bulk nature of observed HTSC in  $\text{La}_2\text{PrNi}_2\text{O}_7$ . Our work thus provides convincing evidence that the bulk HTSC originates from 327-phase-pure bilayer nickelates.

### T-P phase diagram

Figure 4 presents the  $T$ - $P$  phase diagram of  $\text{La}_2\text{PrNi}_2\text{O}_7$ , depicting explicitly the emergence of HTSC in concomitant with the structural transition, similar to  $\text{La}_3\text{Ni}_2\text{O}_{7-\delta}$  (ref. 4) (Extended Data Fig. 8). On increasing pressure,  $T_c^{\text{onset}}$  increases rapidly from 21.4 K at 8 GPa to 82.5 K at 16 GPa and then decreases slightly to 80.4 K at 20 GPa, whereas the highest  $T_c^{\text{zero}}$  reaches about 60 K at 19–20 GPa. It seems that  $T_c(P)$  almost saturates at about 20 GPa and would decrease at higher pressures. The optimal  $T_c^{\text{onset}} = 82.5$  K and  $T_c^{\text{zero}} = 60$  K for  $\text{La}_2\text{PrNi}_2\text{O}_7$  surpasses the corresponding values of  $\text{La}_3\text{Ni}_2\text{O}_{7-\delta}$  at similar pressures. Notably, bulk HTSC occurs at pressures higher than  $P_c \approx 11$  GPa for structural transition, with  $f_{\text{sc}}(8\text{ K})$  increasing rapidly from about 5.3(5)% at 15 GPa to around 97(10)% at 19 GPa. These results indicate that the structural transition is a prerequisite to trigger superconductivity in the bilayer nickelates, whereas bulk HTSC requires higher pressure to further enhance the interlayer coupling between  $3d_{z^2}$  orbitals and to optimize the contribution of Ni- $3d_{z^2}$ -derived  $\gamma$  band near the Fermi level according to recent theoretical investigations<sup>11,12,42,43</sup>. The constructed  $T$ - $P$  phase diagram also shows a close relationship between strange-metal-like behaviour and HTSC in the  $\text{La}_2\text{PrNi}_2\text{O}_7$  samples.

### Conclusion

In summary, we demonstrated that the intergrowth of 327/4310 and 327/214 phases are detrimental to bulk HTSC in the bilayer  $\text{La}_3\text{Ni}_2\text{O}_{7-\delta}$ . By partially replacing La with Pr, we successfully inhibited the intergrowth of 327 with other R-P phases and achieved bulk HTSC with appreciable  $f_{\text{sc}}$  in the high-pressure tetragonal phase of  $\text{La}_2\text{PrNi}_2\text{O}_7$ . The optimal  $T_c^{\text{onset}} = 82.5$  K and  $T_c^{\text{zero}} = 60$  K are the highest values among nickelate superconductors reported so far. Our results indicate that  $\text{La}_2\text{PrNi}_2\text{O}_7$  can be taken as an ideal platform to investigate the mechanism of HTSC for the bilayer nickelates.

### Online content

Any methods, additional references, Nature Portfolio reporting summaries, source data, extended data, supplementary information, acknowledgements, peer review information; details of author contributions and competing interests; and statements of data and code availability are available at <https://doi.org/10.1038/s41586-024-07996-8>.

1. Sun, H. et al. Signatures of superconductivity near 80 K in a nickelate under high pressure. *Nature* **621**, 493–498 (2023).
2. Hou, J. et al. Emergence of high-temperature superconducting phase in pressurized  $\text{La}_3\text{Ni}_2\text{O}_7$  crystals. *Chin. Phys. Lett.* **40**, 117302 (2023).
3. Zhang, Y. et al. High-temperature superconductivity with zero resistance and strange-metal behaviour in  $\text{La}_3\text{Ni}_2\text{O}_{7-\delta}$ . *Nat. Phys.* **20**, 1269–1273 (2024).
4. Wang, G. et al. Pressure-induced superconductivity in polycrystalline  $\text{La}_3\text{Ni}_2\text{O}_{7-\delta}$ . *Phys. Rev. X* **14**, 011040 (2024).
5. Zhou, Y. et al. Investigations of key issues on the reproducibility of high- $T_c$  superconductivity emerging from compressed  $\text{La}_3\text{Ni}_2\text{O}_{7-\delta}$ . Preprint at arxiv.org/abs/2311.12361 (2023).
6. Puphal, P. et al. Unconventional crystal structure of the high-pressure superconductor  $\text{La}_3\text{Ni}_2\text{O}_7$ . *Phys. Rev. Lett.* (in the press).
7. Abadi, S. N. et al. Electronic structure of the alternating monolayer-trilayer phase of  $\text{La}_3\text{Ni}_2\text{O}_7$ . Preprint at arxiv.org/abs/2402.07143 (2024).
8. Chen, X. et al. Polymorphism in the Ruddlesden-Popper nickelate  $\text{La}_3\text{Ni}_2\text{O}_7$ : discovery of a hidden phase with distinctive layer stacking. *J. Am. Chem. Soc.* **146**, 3640–3645 (2024).
9. Wang, H., Chen, L., Rutherford, A., Zhou, H. & Xie, W. Long-range structural order in a hidden phase of Ruddlesden-Popper bilayer nickelate  $\text{La}_3\text{Ni}_2\text{O}_7$ . *Inorg. Chem.* **63**, 5020–5026 (2024).
10. Liu, Z. et al. Electronic correlations and partial gap in the bilayer nickelate  $\text{La}_3\text{Ni}_2\text{O}_7$ . *Nat. Commun.* **15**, 7570 (2024).
11. Luo, Z., Hu, X., Wang, M., Wu, W. & Yao, D.-X. Bilayer two-orbital model of  $\text{La}_3\text{Ni}_2\text{O}_7$  under pressure. *Phys. Rev. Lett.* **131**, 126001 (2023).

12. Christiansson, V., Petocchi, F. & Werner, P. Correlated electronic structure of  $\text{La}_3\text{Ni}_2\text{O}_7$  under pressure. *Phys. Rev. Lett.* **131**, 206501 (2023).
13. Liu, Y.-B., Mei, J.-W., Ye, F., Chen, W.-Q. & Yang, F.  $s^{\pm}$ -Wave pairing and the destructive role of apical-oxygen deficiencies in  $\text{La}_3\text{Ni}_2\text{O}_7$  under pressure. *Phys. Rev. Lett.* **131**, 236002 (2023).
14. Qu, X.-Z. et al. Bilayer  $t$ - $J$ - $J_1$  model and magnetically mediated pairing in the pressurized nickelate  $\text{La}_3\text{Ni}_2\text{O}_7$ . *Phys. Rev. Lett.* **132**, 036502 (2024).
15. Sakakibara, H., Kitamine, N., Ochi, M. & Kuroki, K. Possible high  $T_c$  superconductivity in  $\text{La}_3\text{Ni}_2\text{O}_7$  under high pressure through manifestation of a nearly half-filled bilayer Hubbard model. *Phys. Rev. Lett.* **132**, 106002 (2024).
16. Wang, L. et al. Structure responsible for the superconducting state in  $\text{La}_3\text{Ni}_2\text{O}_7$  at high-pressure and low-temperature conditions. *J. Am. Chem. Soc.* **146**, 7506–7514 (2024).
17. Takegami, D. et al. Absence of  $\text{Ni}^{2+}/\text{Ni}^{3+}$  charge disproportionation and possible roles of  $O$  2p holes in  $\text{La}_3\text{Ni}_2\text{O}_{7-\delta}$  revealed by hard X-ray photoemission spectroscopy. *Phys. Rev. B* **109**, 125119 (2024).
18. Li, Y. D. et al. Ultrafast dynamics of bilayer and trilayer nickelate superconductors. Preprint at arxiv.org/abs/2403.05012 (2024).
19. Dan, Z. et al. Spin-density-wave transition in double-layer nickelate  $\text{La}_3\text{Ni}_2\text{O}_7$ . Preprint at arxiv.org/abs/2402.03952 (2024).
20. Wang, Y., Jiang, K., Wang, Z., Zhang, F.-C. & Hu, J. Electronic structure and superconductivity in bilayer  $\text{La}_3\text{Ni}_2\text{O}_7$ . Preprint at arxiv.org/html/2401.15097v1 (2024).
21. Chen, X. et al. Electronic and magnetic excitations in  $\text{La}_3\text{Ni}_2\text{O}_7$ . Preprint at arxiv.org/abs/2401.12657 (2024).
22. Xie, T. et al. Neutron scattering studies on the high- $T_c$  superconductor  $\text{La}_3\text{Ni}_2\text{O}_{7-\delta}$  at ambient pressure. Preprint at arxiv.org/abs/2401.12635 (2024).
23. Geisler, B. et al. Optical properties and electronic correlations in  $\text{La}_3\text{Ni}_2\text{O}_{7-\delta}$  bilayer nickelates under high pressure. Preprint at arxiv.org/abs/2401.04258 (2023).
24. Dong, Z. et al. Visualization of oxygen vacancies and self-doped ligand holes in  $\text{La}_3\text{Ni}_2\text{O}_{7-\delta}$ . *Nature* **630**, 847–852 (2024).
25. Kakoi, M. et al. Multiband metallic ground state in multilayered nickelates  $\text{La}_3\text{Ni}_2\text{O}_7$  and  $\text{La}_4\text{Ni}_3\text{O}_{10}$  probed by  $^{139}\text{La}$ -NMR at ambient pressure. *J. Phys. Soc. Jpn.* **93**, 053702 (2024).
26. Li, F. et al. Design and synthesis of three-dimensional hybrid Ruddlesden-Popper nickelate single crystals. *Phys. Rev. Mater.* **8**, 053401 (2024).
27. Chen, K. et al. Evidence of spin density waves in  $\text{La}_3\text{Ni}_2\text{O}_{7-\delta}$ . *Phys. Rev. Lett.* **132**, 256503 (2024).
28. Yang, J. et al. Orbital-dependent electron correlation in double-layer nickelate  $\text{La}_3\text{Ni}_2\text{O}_7$ . *Nat. Commun.* **15**, 4373 (2024).
29. Zhang, Y., Lin, L.-F., Moreo, A., Maier, T. A. & Dagotto, E. Structural phase transition,  $s_{\pm}$ -wave pairing, and magnetic stripe order in bilayered superconductor  $\text{La}_3\text{Ni}_2\text{O}_7$  under pressure. *Nat. Commun.* **15**, 2470 (2024).
30. Jiang, R., Hou, J., Fan, Z., Lang, Z.-J. & Ku, W. Pressure driven fractionalization of ionic spins results in cupratelike high- $T_c$  superconductivity in  $\text{La}_3\text{Ni}_2\text{O}_7$ . *Phys. Rev. Lett.* **132**, 126503 (2024).
31. Zhang, J. et al. High oxygen pressure floating zone growth and crystal structure of the metallic nickelates  $R_x\text{Ni}_3\text{O}_{10}$  ( $R=\text{La}, \text{Pr}$ ). *Phys. Rev. Mater.* **4**, 083402 (2020).
32. Zhang, Z. & Greenblatt, M. Synthesis, structure, and properties of  $\text{Ln}_x\text{Ni}_3\text{O}_{10-\delta}$  ( $\text{Ln}=\text{La}, \text{Pr}$ , and Nd). *J. Solid State Chem.* **117**, 236–246 (1995).
33. Liu, Z. et al. Evidence for charge and spin density waves in single crystals of  $\text{La}_3\text{Ni}_2\text{O}_7$  and  $\text{La}_3\text{Ni}_2\text{O}_6$ . *Sci. China Phys. Mech. Astron.* **66**, 217411 (2022).
34. Fukamachi, T., Oda, K., Kobayashi, Y., Miyashita, T. & Sato, M. Studies on successive electronic state changes in systems with  $\text{NiO}_2$  planes –  $^{139}\text{La}$ -NMR/NQR–. *J. Phys. Soc. Jpn.* **70**, 2757–2764 (2001).
35. Gopalan, P., McElfresh, M. W., Käkol, Z., Spalek, J. & Honig, J. M. Influence of oxygen stoichiometry on the antiferromagnetic ordering of single crystals of  $\text{La}_2\text{NiO}_{4-\delta}$ . *Phys. Rev. B* **45**, 249–255 (1992).
36. Buttrey, D. J., Honig, J. M. & Rao, C. N. R. Magnetic properties of quasi-two-dimensional  $\text{La}_2\text{NiO}_4$ . *J. Solid State Chem.* **64**, 287–295 (1986).
37. Wada, S., Kobayashi, T., Kaburagi, M., Shibutani, K. & Ogawa, R.  $^{139}\text{La}$  NQR study of antiferromagnetic  $\text{La}_2\text{NiO}_{4-\delta}$ . *J. Phys. Soc. Jpn.* **58**, 2658–2661 (1989).
38. Sun, J. P. et al. Dome-shaped magnetic order competing with high-temperature superconductivity at high pressures in FeSe. *Nat. Commun.* **7**, 12146 (2016).
39. Sun, J. P. et al. High- $T_c$  superconductivity in FeSe at high pressure: dominant hole carriers and enhanced spin fluctuations. *Phys. Rev. Lett.* **118**, 147004 (2017).
40. Kumar, R. S. et al. Crystal and electronic structure of FeSe at high pressure and low temperature. *J. Phys. Chem. B* **114**, 12597–12606 (2010).
41. Uhoya, W. et al. Simultaneous measurement of pressure evolution of crystal structure and superconductivity in  $\text{FeSe}_{0.92}$  using designer diamonds. *Europhys. Lett.* **99**, 26002 (2012).
42. Lu, C., Pan, Z., Yang, F. & Wu, C. Interlayer-coupling-driven high-temperature superconductivity in  $\text{La}_3\text{Ni}_2\text{O}_7$  under pressure. *Phys. Rev. Lett.* **132**, 146002 (2024).
43. Oh, H. & Zhang, Y.-H. Type-II  $t$ - $J$  model and shared superexchange coupling from Hund's rule in superconducting  $\text{La}_3\text{Ni}_2\text{O}_7$ . *Phys. Rev. B* **108**, 174511 (2023).

**Publisher's note** Springer Nature remains neutral with regard to jurisdictional claims in published maps and institutional affiliations.

Springer Nature or its licensor (e.g. a society or other partner) holds exclusive rights to this article under a publishing agreement with the author(s) or other rightsholder(s); author self-archiving of the accepted manuscript version of this article is solely governed by the terms of such publishing agreement and applicable law.

© The Author(s), under exclusive licence to Springer Nature Limited 2024

## Methods

### Sample synthesis

Poly-crystalline  $\text{La}_{3-x}\text{Pr}_x\text{Ni}_2\text{O}_{7-\delta}$  ( $0 \leq x \leq 1$ ) samples were synthesized using the sol-gel method as described in previous studies<sup>44,45</sup>. Stoichiometric mixtures of  $\text{La}_2\text{O}_3$ ,  $\text{Pr}_6\text{O}_{11}$  and  $\text{Ni}(\text{NO}_3)_2 \cdot 6\text{H}_2\text{O}$ , all of them with a purity of 99.99% from Alfa Aesar, were first dissolved in the deionized water with the addition of an appropriate amount of citric acid and nitric acid, and stirred in a 90 °C water bath for approximately 4 h. Then the obtained vibrant green nitrate gel was subjected to heat treatment overnight at 800 °C to remove excess organic matter. After that, the product was ground, pressed into pellets and sintered in air at 1,100–1,150 °C for 24 h.

### Sample characterizations

The phase purity of  $\text{La}_{3-x}\text{Pr}_x\text{Ni}_2\text{O}_{7-\delta}$  at ambient conditions was determined by XRD collected through a Huber diffractometer with  $\text{Cu K}_\alpha$  radiation. Temperature-dependent resistivity,  $\rho(T)$ , and magnetic susceptibility,  $\chi(T)$ , were measured by using a Quantum Design Physical Properties Measurement System and Magnetic Property Measurement System, respectively. HAADF-STEM observations were performed in a JEOL ARM200F equipped with double-aberration correctors and operated at 200 kV. The STEM sample was prepared by crushing the poly-crystalline into fine fragments. Then the resulting suspensions were dispersed on holey copper grids. TGA measurement was accomplished in NETZSCH STA 449F3, using a 10%  $\text{H}_2/\text{Ar}$  gas flow of 20 ml min<sup>-1</sup> with a 5 K min<sup>-1</sup> rate up to 1,050 K. The  $\text{La}_{3-x}\text{Pr}_x\text{Ni}_2\text{O}_{7-\delta}$  samples tend to absorb moisture in the air; we thus stored the samples in the glove box immediately after taking them out of the furnace. For TGA measurements, we carefully performed the blank tests. After TGA measurements, we measured XRD to confirm that the resultant products are  $\text{La}_2\text{O}_3$ , Ni and  $\text{Pr}_2\text{O}_3$ . The analysis of chemical composition and microstructure used a Hitachi model S-4800 field emission scanning electron microscope equipped with an EDX spectrometer. <sup>139</sup>La-NQR spectra were measured on a powder sample weighing 300 mg by sweeping the frequency point by point and integrating spin-echo intensity.

NPD measurements were performed on the HB-2A diffractometer at the High Flux Isotope Reactor, Oak Ridge National Laboratory. Powder samples of  $\text{La}_{3-x}\text{Pr}_x\text{Ni}_2\text{O}_{7-\delta}$  were contained within a 6-mm-diameter vanadium sample can. Data were collected at 295 K with constant wavelength ( $\lambda = 1.54 \text{ \AA}$ ) measurements performed from the Ge (115) monochromator reflection. The NPD patterns were collected by scanning a 120° bank of 44 <sup>3</sup>He detectors in 0.05° steps to give 2θ coverage from 5° to 150°. Rietveld refinements were performed with the FULLPROF program.

### High-pressure measurements

The high-pressure SXRD of  $\text{La}_2\text{PrNi}_2\text{O}_7$  was measured at the 4W2 beamline at the Beijing Synchrotron Radiation Facility with a wavelength of  $\lambda = 0.6199 \text{ \AA}$ . Rietveld analysis of high-pressure SXRD data was performed with GSAS-II suite<sup>46</sup>. We used the cubic anvil cell and two-stage 6/8 multianvil apparatus to measure  $\rho(T)$  at different pressures up to 15 GPa and 20 GPa, respectively. Glycerol and Fluorinert FC70:FC77 (1:1) were used as the liquid pressure-transmitting medium in the cubic anvil cell and multianvil, respectively. The pressure values inside the cubic anvil cell and multianvil were estimated from pressure-loading force calibration curves determined by measuring the structure phase transitions of Bi, Sn, Pb, ZnS and GaAs at room temperature<sup>47</sup>. The a.c. magnetic susceptibility  $\chi'(T)$  of  $\text{La}_2\text{PrNi}_2\text{O}_7$  samples 3 and 4 under various hydrostatic pressures up to 19 GPa and 20 GPa were measured with the mutual induction method in the multianvil apparatus. The FeSe (refs. 38,39) single crystal was used as a reference for the superconducting diamagnetic signal because the lowest temperature of our multianvil apparatus can reach approximately 8 K, and the volume ratio of FeSe to  $\text{La}_2\text{PrNi}_2\text{O}_7$  is about 1:1.15 for sample 3 and 1:1.5 for sample 4. An excitation current of about 0.1 mA with a frequency of 1,117 Hz was applied to the excitation coil for the  $\chi'(T)$  measurements on sample 3

and about 0.5 mA with a frequency of 732 Hz was applied to the excitation coil for the  $\chi'(T)$  measurements on sample 4, and the output signal was picked up with a Stanford Research SR830 lock-in amplifier. Assuming an  $f_{\text{sc}} = 100\%$  for FeSe at 9 GPa, the  $f_{\text{sc}}$  of  $\text{La}_2\text{PrNi}_2\text{O}_7$  can be estimated through the formula

$$f_{\text{sc}} = [4\chi'(\text{La}_2\text{PrNi}_2\text{O}_7)/4\chi'(\text{FeSe})] \times V_{\text{ratio}} \times 100\%,$$

where  $V_{\text{ratio}}$  is the volume ratio between FeSe and  $\text{La}_2\text{PrNi}_2\text{O}_7$ . Based on the values of  $\Delta\chi'$  shown in Fig. 3e and Extended Data Fig. 7c, the  $f_{\text{sc}}$  of  $\text{La}_2\text{PrNi}_2\text{O}_7$  at different pressures can be calculated. For example, the  $f_{\text{sc}}$  of sample 3 at 19 GPa is calculated as  $f_{\text{sc}} = [(3.28 \times 10^{-5})/(2.95 \times 10^{-5})] \times (1/1.15) \times 100\% \approx 97\%$ . The error bar of  $f_{\text{sc}}$  mainly comes from the uncertainty in determining the volumes of  $\text{La}_2\text{PrNi}_2\text{O}_7$  and FeSe with irregular shapes, having an upper limit of about 10%. This transfers to  $f_{\text{sc}}$  with an error bar of  $97\% \times 10\% = 9.7\%$ , which gives rise to  $f_{\text{sc}}(19 \text{ GPa}) = 97(10)\%$ . The  $\chi'(T)$  measurements did not detect the real Meissner state and the obtained  $f_{\text{sc}}$  values could be a bit overestimated because of the demagnetization effect.

### Data availability

Source data are provided with this paper. Any additional data that support the findings of this study are available from the corresponding author upon reasonable request.

44. Zhang, Z., Greenblatt, M. & Goodenough, J. B. Synthesis, structure, and properties of the layered perovskite  $\text{La}_3\text{Ni}_2\text{O}_{7-\delta}$ . *J. Solid State Chem.* **108**, 402–409 (1994).
45. Chandrasekharan Meenu, P. et al. Electro-oxidation reaction of methanol over  $\text{La}_{2-x}\text{Sr}_x\text{NiO}_{4+\delta}$  Ruddlesden-Popper oxides. *ACS Appl. Energy Mater.* **5**, 503–515 (2022).
46. Toby, B. H. & Von Dreele, R. B. GSAS-II: the genesis of a modern open-source all purpose crystallography software package. *J. Appl. Crystallogr.* **46**, 544–549 (2013).
47. Cheng, J.-G. et al. Integrated-fin gasket for palm cubic-anvil high pressure apparatus. *Rev. Sci. Instrum.* **85**, 093907 (2014).

**Acknowledgements** This work is supported by the National Key Research and Development Program of China (2023YFA1406100, 2021YFA1400200, 2023YFA1607400 and 2022YFA1403402), National Natural Science Foundation of China (12025408, 11921004, U23A6003, U22A6005, 12174424, 12374142, 12304170, 12074414 and 12304075), the Strategic Priority Research Program of CAS (XDB33000000), the Specific Research Assistant Funding Program of CAS (E3VP011X6), the Postdoctoral Fellowship Program of China Postdoctoral Science Foundation (GZB20230828), the China Postdoctoral Science Foundation (2023M743740), CAS PIPI program (2024PG0003) and the Outstanding member of Youth Promotion Association of CAS (Y2022004). J. Hu was supported by the New Cornerstone Investigator Program. J. Yan was supported by the US Department of Energy, Office of Science, Basic Energy Sciences, Division of Materials Sciences and Engineering. The high-pressure transport and the NQR experiments were, respectively, performed at the Cubic Anvil Cell station and the High Field Nuclear Magnetic Resonance station of Synergetic Extreme Condition User Facility. High-pressure synchrotron XRD measurements were performed at the 4W2 High Pressure Station, Beijing Synchrotron Radiation Facility and the BL15U1 station of Shanghai Synchrotron Radiation Facility. This research used resources at the High Flux Isotope Reactor, a US DOE Office of Science User Facility operated by the Oak Ridge National Laboratory.

**Author contributions** J.C. designed and supervised this project. N.W. and G.W. synthesized the materials and characterized their structure using XRD and EDX; N.W., G.W., Y.L., H.Z. and X.D. measured the physical properties at ambient pressure; N.W., G.W. and J. Hou performed high-pressure resistivity measurements by using the cubic anvil cell apparatus with the support of H.M., P.Y., Z.L., J.S. and B.W.; N.W., G.W. and L.S. performed high-pressure SXRD measurements; X.S. J. Hou, S.N., K.K. and Y.U. performed high-pressure resistivity and a.c. magnetic susceptibility measurements by using the multianvil apparatus; N.W., G.W. and J.C. analysed all the collected data; J.L., J.D., J.F., J.Y. and R.Z. carried out the NQR measurements; R.Z. analysed the NQR data; X.M. and H.Y. performed the HAADF-STEM measurements and data analyses; Y.S. and Z.R. measured the TGA data; S.C. and J. Yan measured and analysed the NPD data; Y.W., K.J. and J. Hu gave advice from a theoretical perspective; J.C., N.W., G.W. and R.Z. wrote the paper with inputs from all co-authors.

**Competing interests** The authors declare no competing interests.

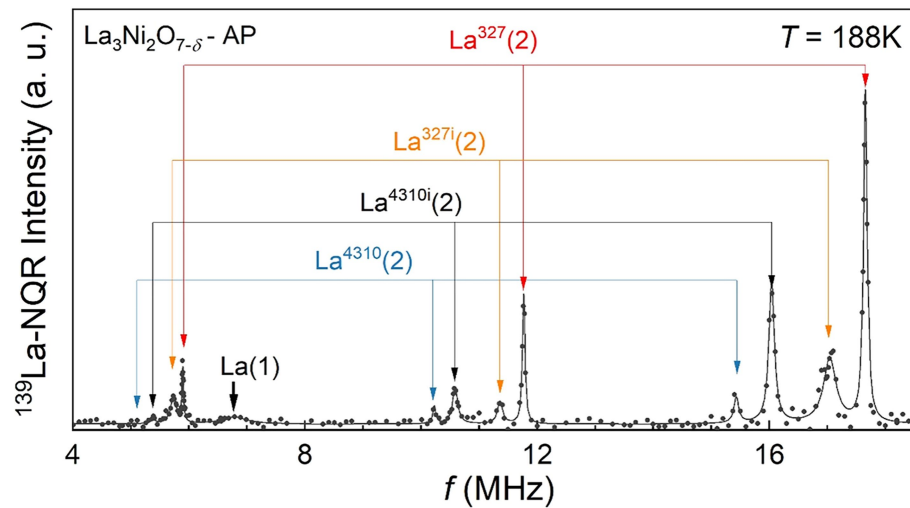
### Additional information

**Supplementary information** The online version contains supplementary material available at <https://doi.org/10.1038/s41586-024-07996-8>.

**Correspondence and requests for materials** should be addressed to Ningning Wang, Rui Zhou, Yoshi Uwatoko or Jinguang Cheng.

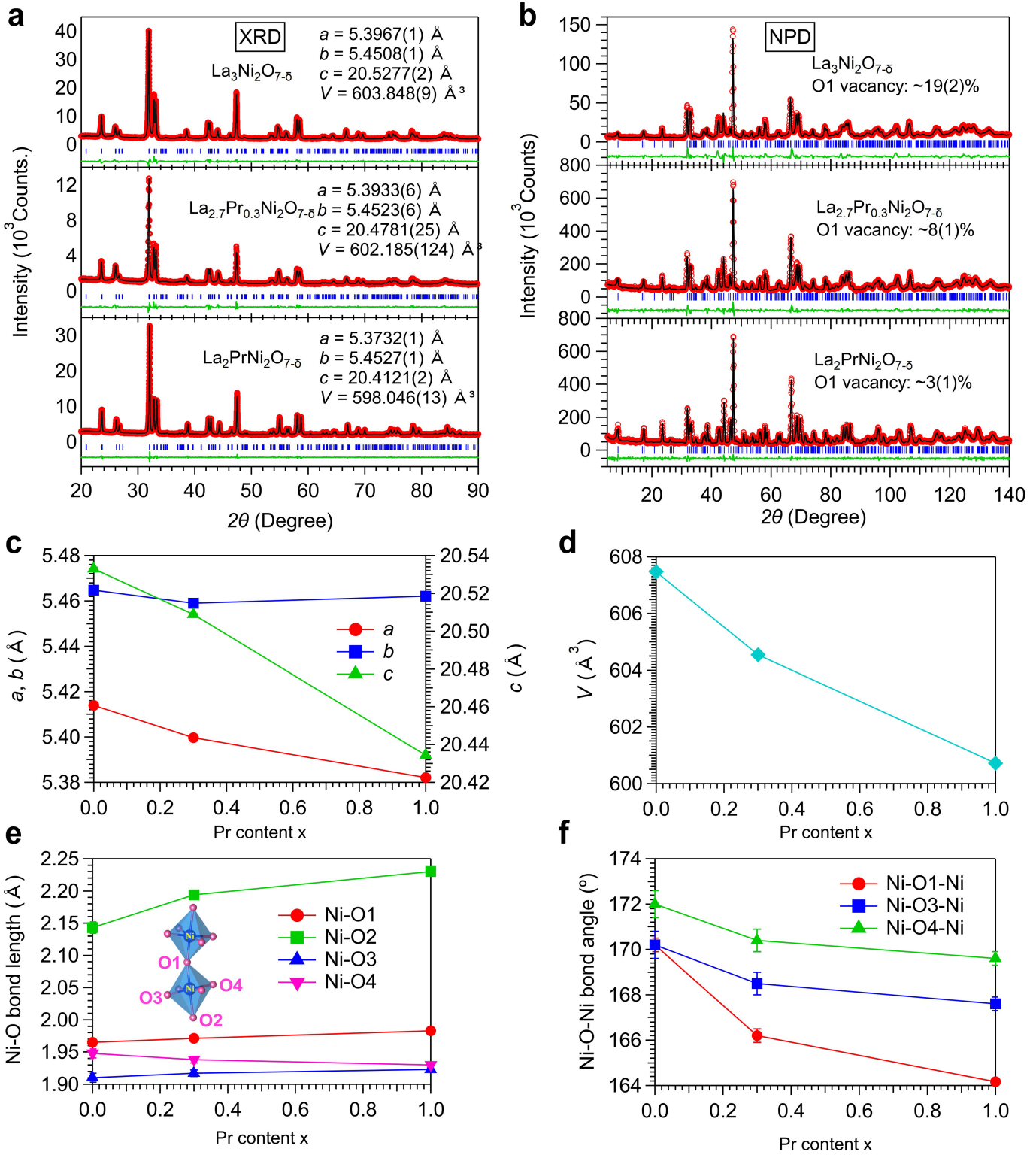
**Peer review information** *Nature* thanks Liangzi Deng, Weiwei Xie and the other, anonymous, reviewer(s) for their contribution to the peer review of this work. Peer reviewer reports are available.

**Reprints and permissions information** is available at <http://www.nature.com/reprints>.


**Extended Data Fig. 1 |  $^{139}\text{La}$ -NQR spectrum for the  $\text{La}_3\text{Ni}_2\text{O}_{7-\delta}$  sample at 188 K.**

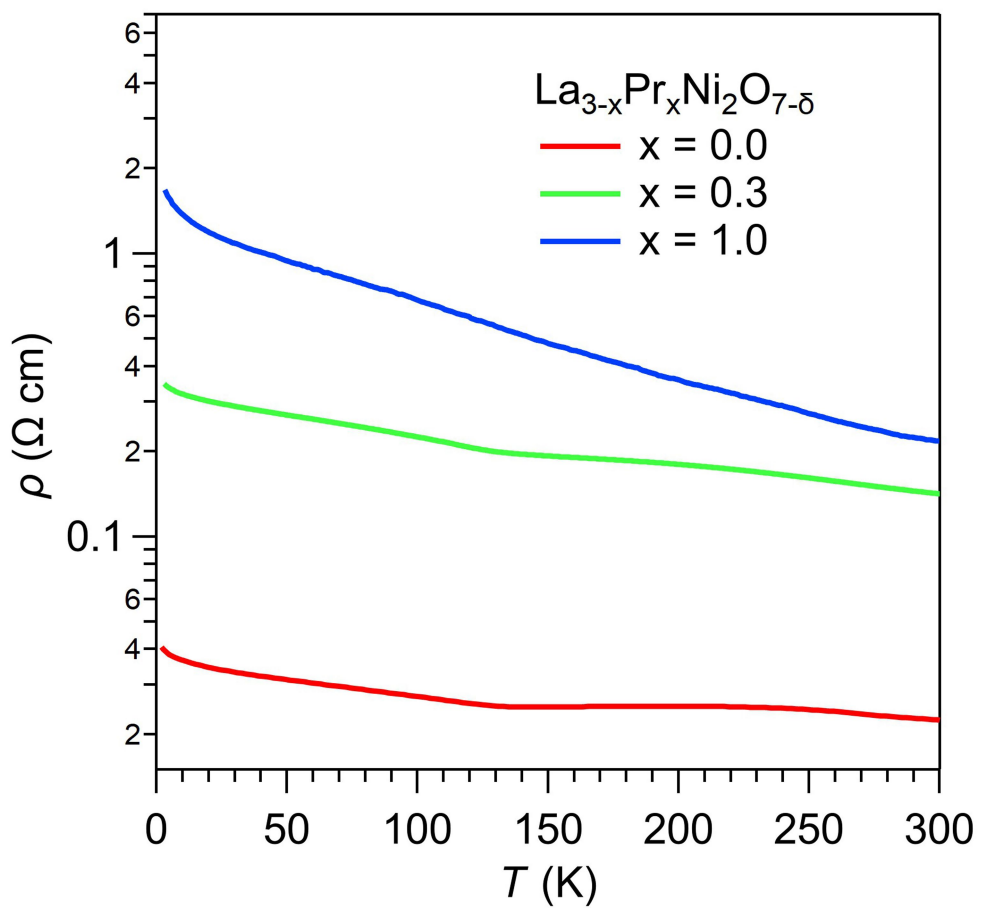
Four distinct pairs of resonance peaks are observed, denoted by four sets of arrows, indicating the existence of four unique  $\text{La}(2)$  sites within the sample.

Owing to a broader linewidth, only one resonance peak corresponding to  $7/2 - 5/2$  transition is observed in the spectrum for the  $\text{La}(1)$  site. The solid lines represent fits obtained using Lorentz functions.

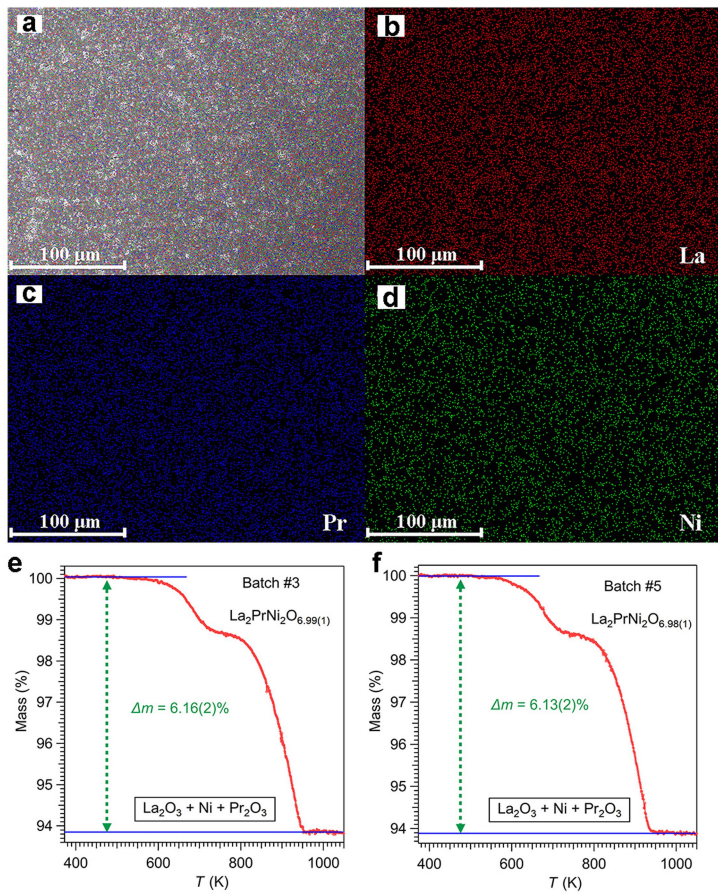


**Extended Data Fig. 2 | Rietveld refinements on the La<sub>3-x</sub>Pr<sub>x</sub>Ni<sub>2</sub>O<sub>7-δ</sub> (x = 0, 0.3, 1.0) samples.** **a,b**, Refinement results of XRD and NPD patterns with the space group *Ama*. **c,d**, The obtained unit-cell parameters and volume as a function of the Pr-content x from the NPD data. **e,f**, Ni-O bond lengths and Ni-O-Ni bond

angles as a function of the Pr-content x from the NPD data. According to the NPD refinement results, no site preference for Pr was detected and the oxygen vacancies at the inner apical O1 sites decrease gradually with increasing the Pr content.

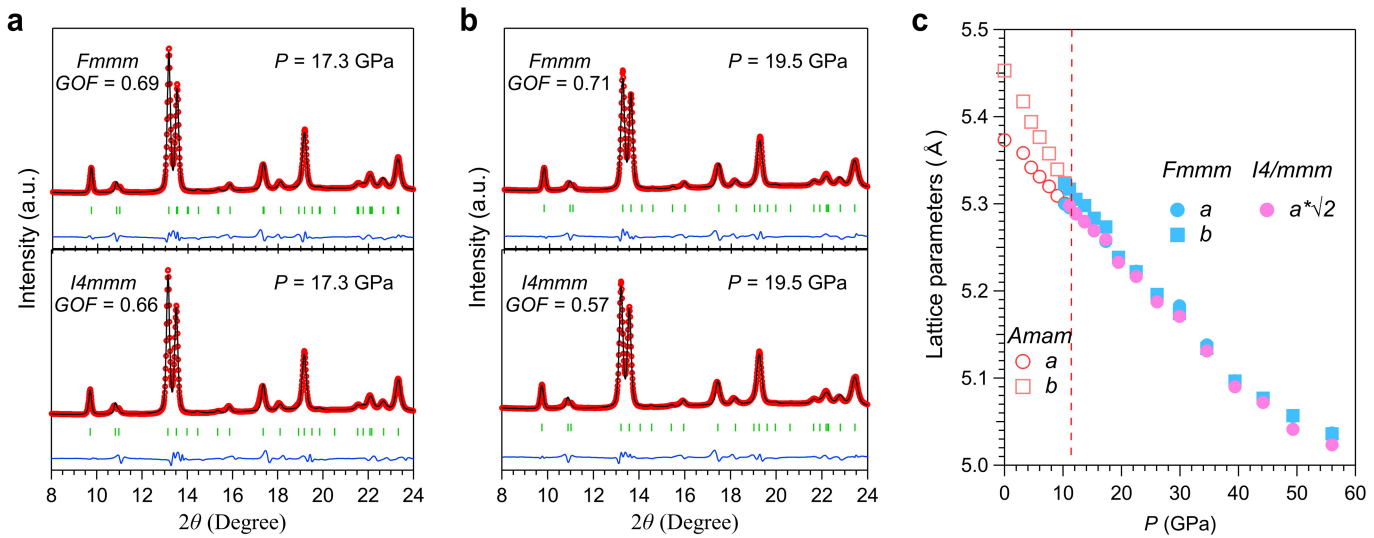


**Extended Data Fig. 3 |  $\rho(T)$  of  $\text{La}_{3-x}\text{Pr}_x\text{Ni}_2\text{O}_{7-\delta}$  at ambient pressure.** Temperature dependence of  $\rho(T)$  increases gradually with increasing the Pr-content  $x$  in the  $\text{La}_{3-x}\text{Pr}_x\text{Ni}_2\text{O}_{7-\delta}$  ( $x = 0, 0.3, 1.0$ ) samples.



**Extended Data Fig. 4 | EDX and TGA results of the  $\text{La}_2\text{PrNi}_2\text{O}_7$  sample.**  
**a–d**, EDX mapping patterns showing the uniform distribution of La, Pr, and Ni elements. Each colour represents a specific element; the mapping image illustrates the spatial distribution of elements within the sample. **e,f**, Analysis

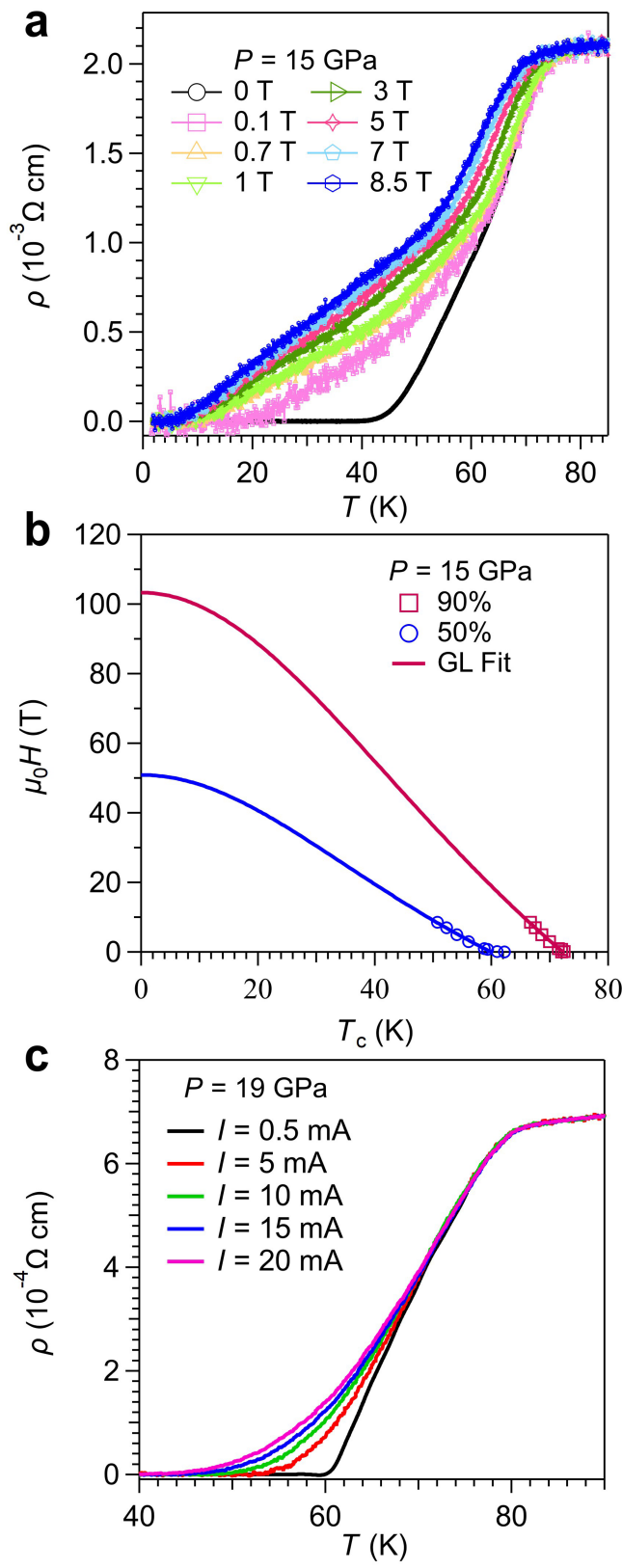
of the TGA data revealed a negligible oxygen deficiency with  $\delta \approx 0.02(1)$  for  $\text{La}_2\text{PrNi}_2\text{O}_{7-\delta}$ , which is smaller than the  $\delta \approx 0.07$  for  $\text{La}_3\text{Ni}_2\text{O}_{7-\delta}$  prepared in the similar conditions. The thermal decomposition behaviour is similar to that in  $\text{La}_3\text{Ni}_2\text{O}_{7-\delta}$ .



**Extended Data Fig. 5 | Refinement results on HP SXRD of  $\text{La}_2\text{PrNi}_2\text{O}_7$ .**

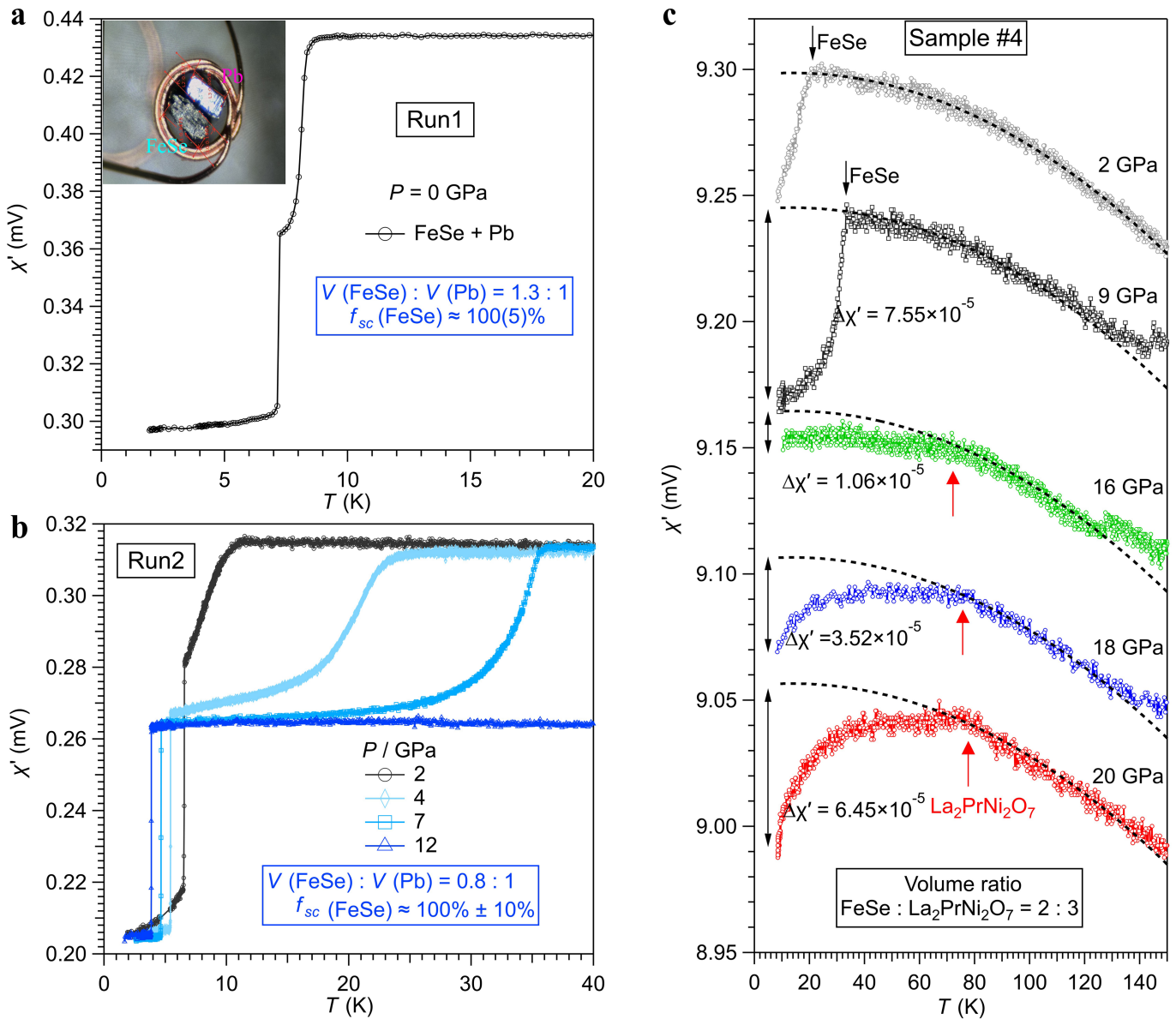
**a,b,** Rietveld refinements on the HP SXRD patterns of  $\text{La}_2\text{PrNi}_2\text{O}_7$  by using orthorhombic  $Fmmm$  and tetragonal  $I4/mmm$  space group under (a) 17.3 GPa and (b) 19.5 GPa. **c,** Comparison of the obtained lattice parameters ( $a$  and  $b$ ) as a

function of the pressure. Although both space groups can refine the data equally well, the refinement results using the orthorhombic  $Fmmm$  space group at higher pressures show that  $a$  and  $b$  merge together, indicating the symmetry of the crystal structure has changed.



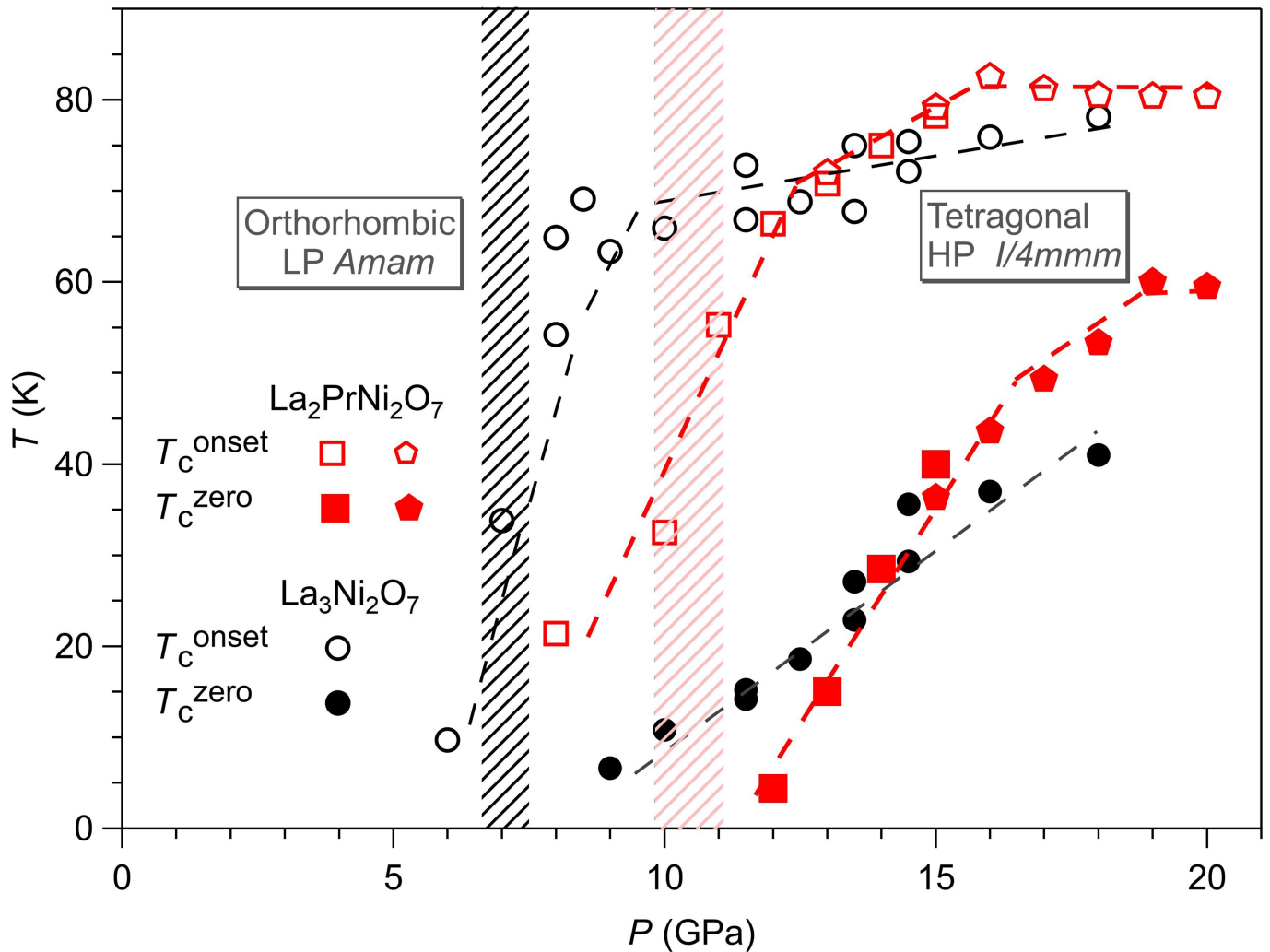
**Extended Data Fig. 6 | Effects of magnetic field and electrical current on the superconducting transition of  $\text{La}_2\text{PrNi}_2\text{O}_7$  under high pressures.**

**a**, The low-temperature  $\rho(T)$  at 15 GPa under various magnetic fields up to 8.5 T. **b**, Temperature dependence of the upper critical field  $\mu_0 H_{c2}(T)$  at 15 GPa. The solid line is the fitting curve by using the formula  $H_{c2} = H_{c2}(0)(1 - t^2)/(1 + t^2)$ , where  $t = T/T_c$ . **c**, The low-temperature  $\rho(T)$  at 19 GPa of sample #2 measured with different currents, which shows that  $T_c^{zero}$  can be gradually inhibited by increasing electrical currents.



**Extended Data Fig. 7 | Ac magnetic susceptibility  $\chi'(T)$  of FeSe single crystal and La<sub>2</sub>PrNi<sub>2</sub>O<sub>7</sub> sample #4.** **a**, The  $\chi'(T)$  data of the FeSe single crystals together with a piece of Pb measured at ambient pressure (Run1) and **b**, under hydrostatic pressures up to 12 GPa with the mutual induction method in CAC (Run2). The inset of **a** shows the photo of the pick-up coil filled with FeSe and Pb for Run1. **c**, The  $\chi'(T)$  of La<sub>2</sub>PrNi<sub>2</sub>O<sub>7</sub> sample #4 together with a piece of FeSe single crystals measured under hydrostatic pressures up to 20 GPa with the mutual induction

method in MA. Note that the  $f_{sc} \sim 57(6)\%$  at 20 GPa observed for this sample is smaller than ~97(10)% at 19 GPa for sample #3. In addition, the superconducting diamagnetic responses of  $\chi'(T)$  around  $T_c$  for these two samples show distinct behaviours. Although these observations indicate some sample-dependent behaviours for the La<sub>2</sub>PrNi<sub>2</sub>O<sub>7</sub> polycrystalline samples, the appreciable  $f_{sc}$  values for these two independent measurements confirm the bulk nature of observed HTSC.



**Extended Data Fig. 8 | T-P phase diagram.** Pressure dependence of  $T_c$  for the  $\text{La}_2\text{PrNi}_2\text{O}_7$  in comparison with that of  $\text{La}_3\text{Ni}_2\text{O}_{7.6}$  polycrystalline samples. The open and filled symbols represent the onset and zero-resistance superconducting transition temperatures of  $\text{La}_2\text{PrNi}_2\text{O}_7$  determined from the

$\rho(T)$  measurements in CAC and MA. The marks for  $\text{La}_3\text{Ni}_2\text{O}_{7.6}$  are taken from our previous study<sup>4</sup>. The initial slope of  $dT_c^{\text{zero}}/dP \sim 10 \text{ K/GPa}$  for  $\text{La}_2\text{PrNi}_2\text{O}_7$  is much larger than that of  $\sim 4.5 \text{ K/GPa}$  for  $\text{La}_3\text{Ni}_2\text{O}_{7.6}$ .

# Article

**Extended Data Table 1 | NQR results of  $\text{La}_3\text{Ni}_2\text{O}_{7-\delta}$  at 188 K**

	$\text{La}^{327}(2)$	$\text{La}^{327-i}(2)$	$\text{La}^{4310-i}(2)$	$\text{La}^{4310}(2)$
$v_Q$ (MHz)	5.886	5.676	5.359	5.174
$\eta$	0.043	0.105	0.155	0.085
Fraction (%)	$40.4 \pm 4.1$	$27.0 \pm 3.0$	$26.0 \pm 2.8$	$6.6 \pm 1.0$

Experimental results of the quadrupole frequency  $v_Q$ , the asymmetry parameter  $\eta$  of the La(2) sites, and the deduced volume fraction from the Lorentz fitting in the upper panel of Fig. 1c for the  $\text{La}_3\text{Ni}_2\text{O}_{7-\delta}$  polycrystalline sample.

**Extended Data Table 2 | NPD refinement results of  $\text{La}_{3-x}\text{Pr}_x\text{Ni}_2\text{O}_{7-\delta}$  ( $x=0.3, 1$ )**

**$\text{La}_{2.7}\text{Pr}_{0.3}\text{Ni}_2\text{O}_{7-\delta}$**

Atom	Wyc	x	y	z	$100U_{\text{iso}}(\text{\AA}^2)$	Occupancy
La1	4c	0.25	0.2503(21)	0.5	0.093(82)	0.225
La2	8g	0.25	0.2495(13)	0.3171(1)	0.513(58)	0.45
Pr1	4c	0.25	0.2503(21)	0.5	0.093(82)	0.025
Pr2	8g	0.25	0.2495(13)	0.3171(1)	0.513(58)	0.05
Ni	8g	0.25	0.2531(14)	0.0954(1)	0.490(35)	0.5
O1	4c	0.25	0.2964(18)	0	0.973(32)	0.231(3)
O2	8g	0.25	0.2082(10)	0.2017(3)	0.973(32)	0.5
O3	8e	0	0.5	0.1048(3)	0.973(32)	0.5
O4	8e	0.5	0	0.0875(2)	0.973(32)	0.5

Lattice parameters:  $a = 5.39968(12) \text{ \AA}$ ,  $b = 5.45906(13) \text{ \AA}$ ,  $c = 20.50879(49) \text{ \AA}$

$R_p = 5.31\%$ ,  $R_{wp} = 6.63\%$ ,  $\chi^2 = 1.76$ ,  $R_{\text{Bragg}} = 4.42$

**$\text{La}_2\text{PrNi}_2\text{O}_7$**

Atom	Wyc	x	y	z	$100U_{\text{iso}}(\text{\AA}^2)$	Occupancy
La1	4c	0.25	0.2483(13)	0.5	0.300(68)	0.167
La2	8g	0.25	0.2583(8)	0.3183(1)	0.615(44)	0.333
Pr1	4c	0.25	0.2483(13)	0.5	0.300(68)	0.083
Pr2	8g	0.25	0.2583(8)	0.3183(1)	0.615(44)	0.167
Ni	8g	0.25	0.2513(8)	0.0961(1)	0.446(25)	0.5
O1	4c	0.25	0.3013(11)	0	0.757(23)	0.242(2)
O2	8g	0.25	0.2076(7)	0.2046(2)	0.757(23)	0.5
O3	8e	0	0.5	0.1063(2)	0.757(23)	0.5
O4	8e	0.5	0	0.0876(2)	0.757(23)	0.5

Lattice parameters:  $a = 5.38206(9) \text{ \AA}$ ,  $b = 5.46208(9) \text{ \AA}$ ,  $c = 20.43435(33) \text{ \AA}$

$R_p = 4.67\%$ ,  $R_{wp} = 5.63\%$ ,  $\chi^2 = 1.25$ ,  $R_{\text{Bragg}} = 2.49$

Crystal structure parameters from the NPD data at 295 K. All these values were extracted from the Rietveld refinements performed by using the FULLPROF program, where the atom occupancy was defined as the site multiplicity of each Wyckoff position divided by the maxima multiplicity of the space group ( $Z=16$ ).